Testosterone Prompted Cardiac Fibrosis in Arrhythmogenic Right Ventricular Cardiomyopathy: Evidence from Clinical to the *in vitro* Human iPSC-derived Engineered Cardiac Spheroids

Hongyi Cheng [1,2,†], *Xinrui Wang* [3,4,†], *Sichong Qian* [5,†], *Yike Zhang* [1], *Jincheng Jiao* [1,6], *Bingyu Zheng* [1], *Yue Zhu* [1], *Hua Xu* [6], *Jia Song* [7], *Feng Zhang* [1,*], *Xiaohong Jiang* [1,*], *Chang Cui* [1,*], *Minglong Chen* [1,2,8]

[1]*Department of Cardiology, The First Affiliated Hospital of Nanjing Medical University, Nanjing, 210029, China*

[2]*Gusu School, Nanjing Medical University, The Affiliated Suzhou Hospital of Nanjing Medical University, Suzhou, 215002, China*

[3]*Medical Research Center, Fujian Maternity and Child Health Hospital, College of Clinical Medicine for Obstetrics & Gynecology and Pediatrics, Fujian Medical University, Fuzhou, Fujian, 350122, China*

[4]*Fujian Key Laboratory of Women and Children's Critical Diseases Research, Fujian Maternity and Child Health Hospital, Fuzhou, Fujian, 350001, China*

[5]*Department of Cardiac Surgery, Anzhen Hospital, Beijing, 100029, China*

[6]*State Key Laboratory of Digital Medical Engineering, School of Biological Science and Medical Engineering, Southeast University, Nanjing, 210096, China*

[7]*Department of Medicine, Section of Cardiovascular Research, Baylor College of Medicine, Houston, TX77030, USA*

[8]*Key Laboratory of Targeted Intervention of Cardiovascular Disease, Collaborative Innovation Center for Cardiovascular Disease Translational Medicine, Nanjing Medical University, Nanjing, 210029, China*

*Corresponding author

E-mail addresses: cuichang@njmu.edu.cn (C. Cui); jiangxiaohong0326@163.com (X. Jiang); 591671366@qq.com (F. Zhang)

[†] These authors contributed equally to this work.

Abstract

Arrhythmogenic Right Ventricular Cardiomyopathy (ARVC) is a progressive disease characterized by adipose and fibrous replacement of the myocardium. Elevated testosterone levels may contribute to the pathological process in ARVC patients. However, the exact contribution of testosterone to cardiac fibrosis in ARVC remains unclear. In this study, we analyzed the gender differences in the distribution of the low-voltage area in an ARVC cohort undergoing an electrophysiological study, and feature selection suggested the potential contribution of gender differences in the low-voltage areas in ARVC patients. Additionally, we established engineered cardiac spheroids models *in vitro* using patient-specific induced pluripotent stem cell derived cardiomyocytes (iPSC-CMs) and fibroblasts (icFBs), and elucidated the pathogenicity of abnormal splicing in the PKP2 gene caused by an intronic mutation. The additional pathogenic validation of the Desmoglein2 (DSG2) point mutation further confirms the reliability of the models. Moreover, testosterone exacerbated the DNA damage in the mutated cardiomyocytes (CMs) and further activated myofibroblasts as a chain reaction. In conclusion, we designed and constructed an *in vitro* 3D engineered cardiac spheroid model of ARVC based on clinical findings and provided direct evidence of the fibrotic role of testosterone in ARVC.

Key Words: ARVC, Gender Difference, Cardiac Spheroids, Testosterone, Fibrosis

Introduction

Arrhythmogenic right ventricular cardiomyopathy (ARVC) is an inherited cardiomyopathy primarily attributed to mutations in desmosomal protein-encoding genes, notably Plakophilin2 (PKP2), Desmoplakin (DSP), Desmoglein2 (DSG2), Desmocollin2 (DSC2), and Plakoglobin (PKG). The prevalence of ARVC is ~1:2,000 to 1:5,000, depending on geographic location[1]. Clinically, ARVC is marked by the adipose and fibrous degeneration of myocardial tissue, and manifests of ARVC include arrhythmogenic syncope, sustained ventricular tachycardia (VT), and sudden cardiac death[2, 3]. Finally, up to 50% of ARVC patients may develop heart failure[4].

Epidemiological studies suggest that ARVC is more prevalent in males than females[5]. Male patients also face higher risks of ventricular tachycardia/ventricular fibrillation (VT/VF) or death. A previous study has shown that testosterone is an essential factor leading to malignant arrhythmias and an increased risk of major adverse cardiac events (MACE) in male patients with ARVC[6]. Testosterone can increase cardiomyocyte apoptosis and excessive adipogenesis[6]. However, the role of testosterone in the fibrotic process of ARVC remains unclear.

Disease-specific induced pluripotent stem cells drived cardiomyocytes (iPSC-CMs) have successfully replicated the critical features of ARVC, including progressive myocardial cell apoptosis, adipogenesis, and abnormal calcium handlings[6-8]. However, the monolayer culture of CMs leads to cellular disorientation, lacks extracellular matrix, and exhibits limited interactions among various cell types.[9], which may obscure contributions from various cardiac stromal cells[10]. Fabricated cardiac microtissues like organoids and engineered cardiac tissues have been leveraged over the past several years to construct disease models, predict drug toxicity, and assess metabolic properties[11]. Hence, developing an advanced cardiac tissue model *in vitro* would be highly beneficial for investigating the pathology of ARVC.

In this article, we detected a potential impact of gender on low-voltage areas in clinical ARVC patient electrophysiological mapping. Considering that low-voltage areas serve as surrogate markers for cardiac fibrosis [12], we hypothesized that testosterone may promote cardiac fibrosis in ARVC. We obtained disease-specific iPSCs from two ARVC patients and differentiated them into cardiac fibroblasts (icFBs) and ventricular cardiomyocytes (VCMs). Subsequently, we established an engineered cardiac spheroid model and successfully replicated ARVC-related phenotypes *in vitro*. Furthermore, we introduced dihydrotestosterone (DHT) and evaluated its role in the fibrotic process of the ARVC model. Finally, we conducted a preliminary exploration of the mechanisms by which DHT promotes ARVC cardiomyocyte fibrosis.

Materials and methods

ARVC patients and Electroanatomic mapping

We enrolled 60 consecutive patients diagnosed with ARVC who were scheduled to undergo electrophysiological examination or catheter ablation. Electroanatomic mapping was performed using the Ensite system (Abbott Inc.) or the CARTO mapping system (Biosense Webster Inc.). For mapping, we utilized a deflectable duo-decapolar catheter (Livewire, 2-2-2 mm spacing, St. Jude Medical) or an ablation catheter

(Thermocool, Biosense Webster Inc; Coolflex, Abbott Inc). Areas exhibiting a bipolar electrogram amplitude below 0.5 mV were defined as "low-voltage areas." In patients who underwent endocardial and epicardial substrate mapping, 19 showed abnormal substrate in the right ventricular free wall. The study protocol adhered to the ethical guidelines set forth in the 1975 Declaration of Helsinki and received prior approval from the ethics committee of the First Affiliated Hospital of Nanjing Medical University.

Cell Culture and Differentiation

Two iPSC lines used in this study were derived from two ARVC patients with PKP2 mutation c.336+1G>A (PKP2m) or DSG2 mutation 1592T>G (DSG2m) from a previous study[12], respectively. One of their healthy family members was used as the corresponding Control-iPSC line respectively. The Ethics Committee of the First Affiliated Hospital of Nanjing Medical University provided the approval of the study. The iPSC lines were generated using a CytoTune-iPS 2.0 Sendai reprogramming kit (Thermo Fisher Scientific, A16517), which employed four Yamanaka factors (OCT4, KLF4, SOX2, and cMYC), following the manufacturer's instructions with subtle adjustments. Individual colonies were identified and maintained in mTeSR1 Medium (STEMCELL, 85850). The mutation site was examined using Sanger sequencing.

For cardiac differentiation. In accordance with our previous protocol[13], two ARVC-iPSC lines and corresponding Control-iPSC lines underwent cardiac differentiation towards the ventricular myocyte lineage. Briefly, the confluence of iPSCs reached approximately 90% on D0. On D0 to D1, additional CHIR-99021 (6 μmol/L, Selleck, S1263) was added to induce mesodermal differentiation. On D3 to D4, IWR-1 (5 μmol/L, Sigma-Aldrich, I0161) was added to the medium to inhibit Wnt signaling and induce cardiogenesis. From D5 to D7, BMS493 (1 μmol/L, Sigma-Aldrich, B6688) was added for directly differentiating into ventricular cardiomyocytes. From D0 to D7, the basic medium was RPMI 1640 medium (Gibco, C11875500BT) containing B27 minus-insulin supplement (Gibco, A1895601). From D8 onwards, cells were cultured in RPMI 1640 medium containing B-27 complete supplement (Gibco, 17504044). Beating cardiomyocytes were observed on D8 to D10. Besides, to obtain enriched cardiomyocyte populations, glucose-free DMEM (Gibco, 11966025) medium supplemented with 4 mmol/L Sodium L-lactate (Sigma-Aldrich, 71718) and 3.6 mmol/L HEPES (Sigma-Aldrich) were applied for 3-4 days. Purified myocardium was maintained in advanced DMEM/F12 (Gibco, 12634028) supplemented with 2% FBS (Gibco, 10099141). The splicing site was examined using Sanger sequencing. The extracted RNA from Control-VCMs and PKP2m-VCMs was reverse transcribed into cDNA, followed by PCR amplification. Gel electrophoresis was performed, and the amplified cDNA fragments corresponding to EXON1~3 were purified after gel excision.

For icFBs differentiation. Follow the method described earlier[14]. Control-iPSCs reached a confluence of approximately 50% on D0. On D0 to D1, additional CHIR-99021 (6 μmol/L, Selleck) was added and On D3 to D4, IWR-1 (5 μmol/L, Sigma-Aldrich, Germany) was added. On D4, human induced pluripotent stem cell-derived cardiac progenitor cells (iPSC-CPCs) were cultured in advanced DMEM/F12 medium for 24h and re-plated at a density of 20,000 cells/cm^2 and treated with 5 μmol/L of

CHIR-99021 and 2 μmol/L of retinoic acid (S1653, Selleck) for 2 days, and recovered in advanced DMEM/F12 for 3 days. On D8, human induced pluripotent stem cell-derived epicardial cells (iPSC-EPCs) were replated and treated with 10 ng/L of FGF2 (100-18B, PeproTech) and 10 μmol/L of SB431542 (S1067, Selleck chemicals) in Fibroblast Medium-2 (FM2, ScienCell, 2331) for another 5-6 days to harvest icFBs. And icFBs were maintained in FM2 as seed cells of spheroids construction and transwell co-culture model.

Cardiac spheroids generation

Cardiac spheroids use the scaffolded construction method described earlier[15]. Briefly, Collagen type I from rat tail (Corning, 354249) and Geltrex (LDEV-Free, Gibco, A1413301) mix was used to fabricate cardiac spheroids. The final concentrations were collagen I (3 mg/mL), Geltrex (0.08 mg/mL), 2.3% 1M NaOH, and 1×10^{7} total cells/mL consisting of 85% cardiomyocytes and 15% icFBs. A volume of 1 μl of this cocktail was seeded into a low adhesion U-bottom 96-well plate (SpheroX™ 96Ukit, EFL-SP101). Spheroids were maintained in RPMI 1640 medium supplemented with 3% FBS and complete B27 supplement until contractile (D7) and structural (D14) analysis.

Analysis of contraction physiology of spheroids

Spheroids in U-bottle 96-well plate were monitored daily for a spontaneous beating by acquiring representative videos. All videos collected in our experiment were shot at a fixed frame rate of 15 frames/s under the same light intensity. The beating velocity was characterized using custom-built motion tracking software[16] by analyzing videos taken by a bright-field inverted microscope with a CMOS camera (E3CMOS, TOUPTEK PHOTONICS CO., LTD)[17]. The beating velocity is obtained by matching a block of pixels with an identically sized block of pixels in the neighboring frame and capturing the corresponding motion vector data. Subsequently, the tracings of the beating velocity are determined based on the known temporal interval between frames. The procedure to derive the beating velocity involves correlating a set of pixels in a given frame with a corresponding set of pixels in the subsequent frame.

Intracellular calcium transient

Spheroids were loaded with the calcium-sensitive dye Fluo-4 AM (Invitrogen, F14201) at a working concentration of 5 μmol/L for 60 minutes at 37 °C. Spheroids were rinsed and then maintained in Tyrode's solution. The spontaneous calcium fluorescence signal was recorded by an inverted fluorescence microscope (Axio Vert A1, Carl Zeiss, Germany) equipped with an sCMOS camera (Tucsen, Dhyana95, China). Recordings were obtained at the acquisition rate of 70+ frames/second to get original videos. The fluorescence intensity in the region of interest was determined based on the (F-F0)/F0, and a time series analysis was carried out. F0 is the initial background fluorescence intensity, while F is the intensity at any point in time. All calcium transient videos were analyzed using the Time Series Analyzer V3 plugin in ImageJ.

Co-culture Protocol and drug treatment

icFBs and PKP2m-icFBs were co-cultured with PKP2m-VCMs and Control-VCMs, respectively, in Transwell inserts (membrane pore size of 0.4 μm, JET BIOFIL, TCS001012). Adipogenesis medium (Cyagen, HUXXC-90031), with or without 50nM DHT (Selleck, S4757), was added to both the apical and basolateral sides of the Transwells. Control samples were supplemented with ddH_2O or 0.1%DMSO, depending on the solvent used to prepare the concentrated stock. After co-culturing in the Transwell for 48 hours, RNA was extracted from icFBs for qPCR analysis. Additionally, icFBs used for immunofluorescence staining and ROS detection were subjected to an extra 3-day co-culture period.

Immunofluorescence and antibodies

Cells were seeded on a coverslip and cultured for 7 days before being fixed in 4% paraformaldehyde for 30 minutes. The cells were permeabilized with 0.2% Triton X-100 for 3 minutes and then blocked in 3% BSA in PBS for 30 minutes at room temperature. Cells were then incubated overnight at 4 °C with primary antibodies. For iPSCs, anti-TRA-1-60 (1:200 dilution; CST, #4746) and anti-Nanog (1:200 dilution; CST, #4903) were applied. For CMs, anti-α-actinin (1:200 dilution; Sigma-Aldrich, A5044), anti-cardiac troponin I (1:500 dilution; Abcam, ab92547), anti-cardiac troponin T (1:100 dilution; Abcam, ab8295), anti-PKP2 (1:200 dilution; Abcam, ab223757), and anti-γH2AX (1:100 dilution; Abcam, ab11174) were used. For icFBs, anti-Vimentin (1:200 dilution; Abcam, ab47003), anti-γH2AX, and anti-α-SMA (1:200 dilution; Abcam, ab5694) were used. The primary antibodies are listed in Table S1.

Alexa Fluor 488 labeled Donkey anti-Rabbit IgG (1:500 dilution; Yeasen, 34206ES), Alexa Fluor 488 labeled Donkey anti-Mouse IgG (1:500 dilution; Yeasen, 34106ES), and Alexa Fluor 594 labeled Donkey anti-Mouse IgG (1:500 dilution; Yeasen, 34112ES) were used for secondary antibodies. Secondary antibodies were incubated with samples at room temperature for 60 minutes. Phalloidin-California Red Conjugate (APExBIO, B8325) was used to detect the F-actin of EPCs and icFBs. The nuclei were stained with DAPI (Beyotime, C1002) for 1 minute. The cells were imaged under a fluorescence microscope (AxioImager A2, Carl Zeiss, Germany). Images were analyzed and merged with ImageJ (NIH, version 1.8.0_77).

Transmission electron microscopy (TEM)

The cells were fixed with 2.5% glutaraldehyde and 1% osmium tetroxide. After rinsing with PBS, the cells were dehydrated using ethanol solutions and embedded in resin. Ultrathin sections were cut using an ultramicrotome (EMUC7; Leica, Germany) and stained with lead citrate. Visualization was performed using a transmission electron microscope equipped with a CCD camera operating at 75 kV (JEM-1010, Jeol Ltd, Japan).

ROS detection and Flow cytometry

ROS levels were determined using the DCFH-DA (2',7'-Dichlorodihydrofluorescein diacetate) probe (Beyotime, S0033) following the manufacturer's protocol. Briefly, intracellular ROS can oxidize non-fluorescent DCFH (2',7'-Dichlorodihydrofluorescein) to produce fluorescent DCF. The intracellular ROS level was analyzed by inverted fluorescence microscopy and flow cytometry. The Transwell inserts containing icFBs were rinsed with PBS and placed onto glass slides, followed by visualization using an inverted fluorescence microscope (Axio Vert A1, Carl Zeiss, Germany). The cells were analyzed for flow cytometry using FACSCalibur™ (BD, USA), and subsequent analyses were performed using FlowJo software (Tree Star, version 10.5.3).

Real-Time qPCR analysis

Gene expression was quantified using real-time qPCR analysis. On Day 28 of differentiation, PKP2m-VCMs and Control-VCMs were sacrificed for the Real-Time qPCR analysis. qPCR was performed on icFBs co-cultured with VCMs after 48h Transwell co-culture. Total RNA from tissues or cells was extracted using Trizol (Invitrogen, 15596026) following the manufacturer's protocol, quantified by using NanoDrop, and reverse transcribed into cDNA using a cDNA synthesis kit (Yeasen, 11141ES60). qPCR was done with a Step one plus Real-Time PCR system (Applied Biosystems, USA) with gene-specific primers. The amount of RNA was calculated using the comparative threshold cycle method. The mRNA expression levels were normalized to the GAPDH using the $2^{-\Delta\Delta Ct}$ method. All primers were custom-made by Tsingke Biotech Co., Ltd. The primer sequences are shown in Table S2.

Statistical analysis

For statistics of clinical baseline data, data with a normal distribution were presented as the mean±SD. Feature selection was performed in the discovery cohort by using the maximal information coefficient (MIC) algorithm with the low-voltage areas via epicardial mapping and endocardial mapping as the target data, respectively. R software (Version 4.1.0) was used for statistical analyses and data visualization. The *minerva* package (https://search.r-project.org/CRAN/refmans/metrica/html/MIC.html) was used to perform Feature selection[18]. For the *in vitro* experiment part. Data with a normal distribution were presented as the mean±SEM. Students' t-tests were then used to compare two groups. One-way analysis of variance was used to compare multiple groups. The *Chi-square* test was used for categorical variables. All statistical analyses were performed with GraphPad Prism 9 (GraphPad Software, USA). Significance levels were determined by $^*p < 0.05$, $^{**}p < 0.01$, and $^{***}p < 0.001$.

Results

Feature selection suggested the potential influence of gender differences on the low-voltage areas in ARVC patients

To evaluate the contributors of the lesions in ARVC patients, we analyzed a retrospective cohort of ARVC in our medical center, in which 19 patients underwent 3D electrophysiological substrate mapping and exhibited massive areas of low voltage (Table S3). It is evident that males have a relatively big size and percentage of low-voltage area, but differences were relatively small in magnitude. The representative endocardial and epicardial substrate mappings revealed a female ARVC patient with moderate low-voltage area and a male ARVC patient with extensive low-voltage area

(Figure 1a). Additionally, the low-voltage area in the epicardium is more significant than that in the endocardium. We then applied a supervised machine learning method, i.e., feature selection, to analyze the contributors of the endocardial and the epicardial low-voltage areas, respectively. The 14 most important features are listed in Figure 1b. Left ventricular end-diastolic dimension (LVDd) and age were the top two relevant features with the target data. The gender difference was ranked 6th and 4th important feature, respectively. Figure 1c shows the relationship between the low voltage area of substrate mapping and fibrotic myocardial tissue. Considering the relationship between gender differences and cardiac fibrosis in ARVC patients is currently poorly studied, we focused on the association of testosterone, the most important male sex hormone, with the pathological process of cardiac fibrosis in ARVC *in vitro*.

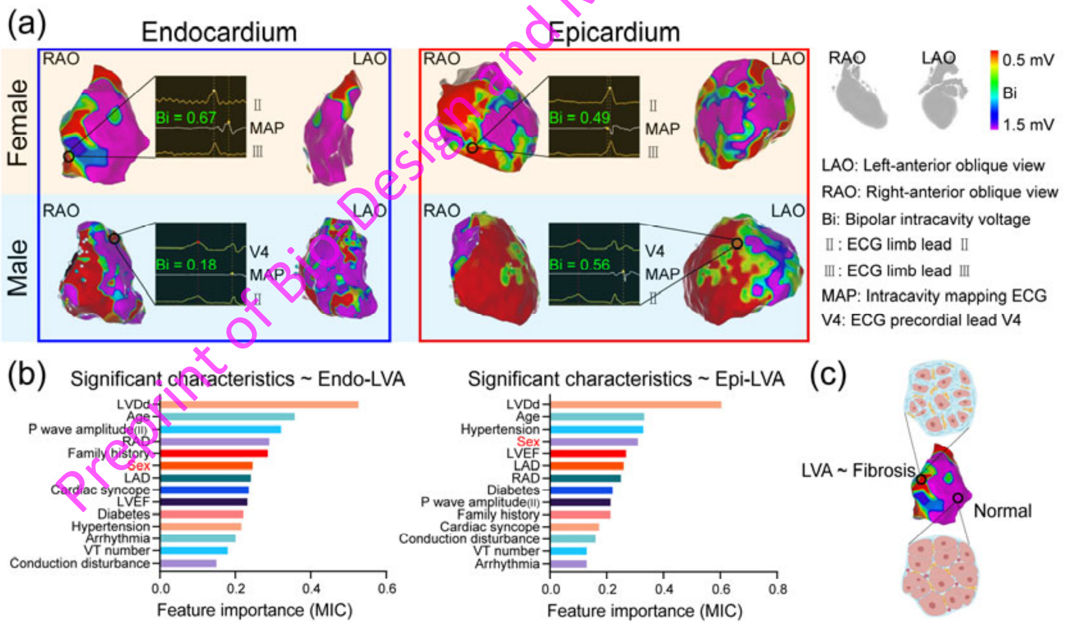

Figure 1 Substrate mapping and clinical features of an ARVC cohort. Endocardial and epicardial substrate mapping shows (a) one female ARVC patient with a moderate low-voltage area and one male ARVC patient with an extensive low-voltage area. (b) Feature selection in the ARVC cohort. The 14 most important features regarding the low voltage areas on both the endocardium and epicardium. (c) Schematic diagram of the relationship between the LVA of substrate mapping and fibrotic myocardial tissue. *Abbreviation*: LVA, Low voltage area; LVDd, Left ventricular end-

diastolic dimension; RAD, Right atrial diameter; LAD, Left atrial diameter; LVEF, Left ventricular ejection fractions; VT, Ventricular tachycardia.

3D Spheroids enabled biomimetic modeling of ARVC

We first generated the PKP2m-iPSC line and DSG2m-iPSC line derived from ARVC patients, respectively, with their corresponding Control-iPSC line derived from an unaffected family member. The mutation sites in the genomic DNA were validated by Sanger sequencing (Figure S1a). The pluripotency of four iPSC lines was confirmed by immunofluorescence staining of Nanog and TRA-1-60 (Figure S1b). Subsequently, the differentiation to VCMs of four iPSC lines was performed. The differentiation into icFBs was performed on the PKP2m-iPSC line and the corresponding Control-iPSC line. The differentiation protocols for VCMs and icFBs, along with representative bright-field images at different stages of differentiation, were depicted in Figure S2a and Figure S2c, respectively. Control-VCMs and ARVC-VCMs all exhibited expression of cardiac markers cTnI and α-actinin (Figure S2b). Figure S2d and Figure S2e showed the cellular morphology of epicardial progenitor cells (EPC) before icFB differentiation, the cytoskeletal morphology of icFBs, and the expression of the marker protein Vimentin. In addition, ARVC-VCMs have a characteristic phenotype of increased lipogenesis in both PKP2m-VCMs and DSG2m-VCMs. Figure S3 showed the characterization of adipogenesis in PKP2m-VCMs, DSG2m-VCMs, and corresponding Control-VCMs. Figure S3a illustrated the up-regulation in the adipogenesis-related gene expressions (*SOX2*, *CTGF*, *FABP4*, *PPARα*) observed under adipogenic culture conditions. The application of Nile Red staining fluorescence images reveals the formation of intracellular lipid droplets, indicating an increased quantity of lipid droplets within ARVC-VCMs (Figure S3b).

We then generated 3D cardiac spheroids by incorporating an extracellular matrix using type I rat tail collagen and Matrigel. The day of spheroids fabrication was designated as D0. Figure 2a depicted the self-assembly and compaction of two kinds of ARVC-spheroids with PKP2 mutation (PKP2m-spheroids) and DSG2 mutation (DSG2m-spheroids) and their corresponding Control-spheroids from D0 to D7. Calcein-PI staining confirmed the good cell viability in all types of spheroids (Figure 2b). As the spheroids self-assembled, PKP2m-spheroids and DSG2m-spheroids exhibited higher compaction and smaller diameters than corresponding Control-spheroids (Figure 2c). We performed a roundness analysis to assess the shape characteristics of the spheroids on D7, revealing that ARVC-spheroids exhibited a relatively more irregular shape (Figure 2d). Representative bright field videos were recorded (Supplementary video1), and the beating behaviors of the cardiac tissues were analyzed. The spontaneous beating frequency was higher in PKP2m-spheroids than in corresponding Control-spheroids, but both decreased over time (Figure 2e). Whereas the spontaneous beating frequency of DSG2m-spheroids increased a little (Figure 2f). Figure S4 displayed the representative beating behavior maps and color-coded heat maps of PKP2m-spheroid, DSG2m-spheroid, and corresponding Control-spheroid during one beat cycle on D7. The length of the arrow in the picture is proportional to the rate of contraction. Control-spheroids exhibited distinct contraction-relaxation directionality, while the beating characteristic of ARVC-spheroids was less pronounced and less consistent in direction. We analyzed three randomly selected areas at the edge of each spheroid and quantified the beating contraction rate velocity. Two kinds of control spheroids displayed synchronized beating trajectories and had a larger maximum contraction rate velocity (Figure 2g). In contrast, the ARVC-spheroids exhibited faster beating frequency, and the beating characteristic varied across different regions (Figure 2h, i).

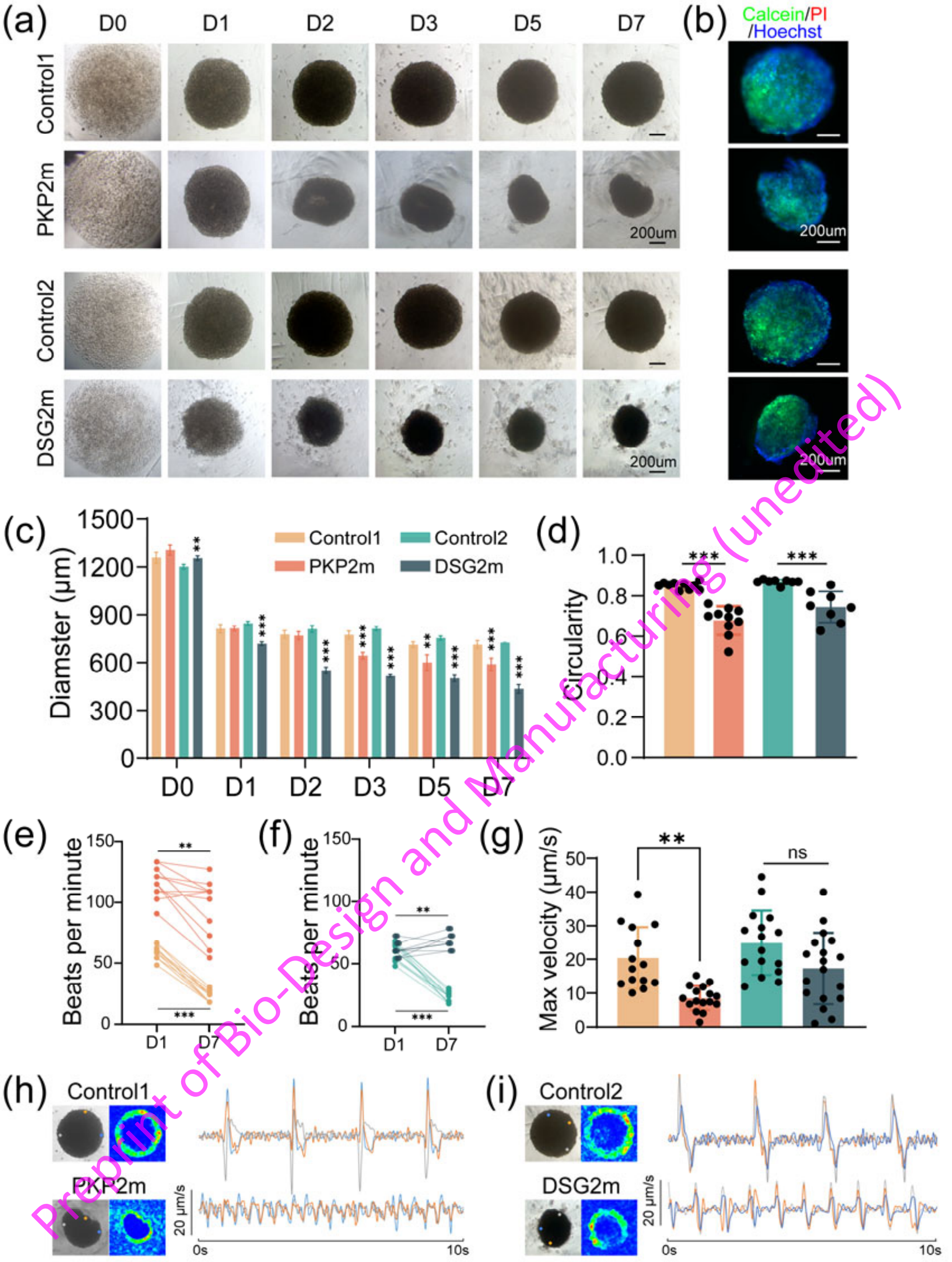

Figure 2 The formation and characteristics of 3D cardiac spheroids.

(a) Representative bright-field images from D0 to D7 showing the self-assembly process of both PKP2m-Spheroids and DSG2m-Spheroids and corresponding Control-Spheroids. Bar=200 μm. (b) Representative live/dead staining of formed Spheroids. Calcein (green), PI (red), and Nucleus (blue). Bar=200 μm. (c) Quantification of Spheroids compaction on the indicated days of culture. $^{**}P<0.01$, $^{***}P<0.001$ compared with corresponding control. (d) The Circularity of PKP2m-Spheroids and DSG2m-Spheroids and corresponding Control-Spheroids. $^{***}P<0.001$. (e, f) The Beats frequency of PKP2m-Spheroids and DSG2m-Spheroids and corresponding Control-Spheroids. (g) The max velocity of PKP2m-Spheroids and DSG2m-Spheroids and corresponding Control-Spheroids. **P<0.01. h, i) Representative spontaneous trace of PKP2m-Spheroids and DSG2m-Spheroids and corresponding Control-Spheroids.

DHT exacerbated fibrosis in ARVC spheroids

To evaluate the role of DHT in the fibrosis process of ARVC, two kinds of ARVC-spheroids and their corresponding Control-spheroids were cultured for an extra 7 days with or without the addition of DHT in the adipogenic medium, starting from the D7 of spheroids construction.

Figure 3a, b showed the representative trace of PKP2m-Spheroid and DSG2m-Spheroid, cultured with or without DHT. It was observed that the cultured in the adipogenic medium increased proarrhythmic events in PKP2m-spheroids and induced the asynchrony of beating. While DSG2m-spheroids appeared in no more incidents (Figure 3c, d). However, additional DHT in the medium significantly increased proarrhythmic events in PKP2m-spheroids and DSG2m-spheroids (Figure 3c, d), and the extra DHT impaired the maximum contraction rate of both ARVC-spheroids (Figure 3e, f).

Immunofluorescent staining of fibrosis was performed on ARVC-spheroids and corresponding Control-spheroids (Figure 3g, h). The results demonstrated that the DHT treatment did not significantly increase the expression of α-SMA in corresponding Control-spheroids, but it significantly enhanced the expression of α-SMA in PKP2m-spheroids (fold changes 3.54±0.45 vs 2.03±0.25, plus DHT or not) and DSG2m-spheroids (fold changes 2.90±0.25 vs 1.37±0.18, plus DHT or not) (Figure 3i).

Furthermore, none of the treatments significantly impacted the expression of Vimentin in PKP2m-spheroids and corresponding Control-spheroids (Figure S5a, b). These findings suggested that fibrosis is primarily caused by the activation of fibroblasts into myofibroblasts within the spheroids rather than the proliferation. The calcium transient analysis demonstrated that Control-spheroids treated with DHT exhibited higher peak amplitudes than PKP2m-spheroids. However, DHT treatment caused altered Ca^{2+} handling in PKP2m-spheroids (Figure 3j) and resulted in a higher occurrence of proarrhythmic events (Figure 3k).

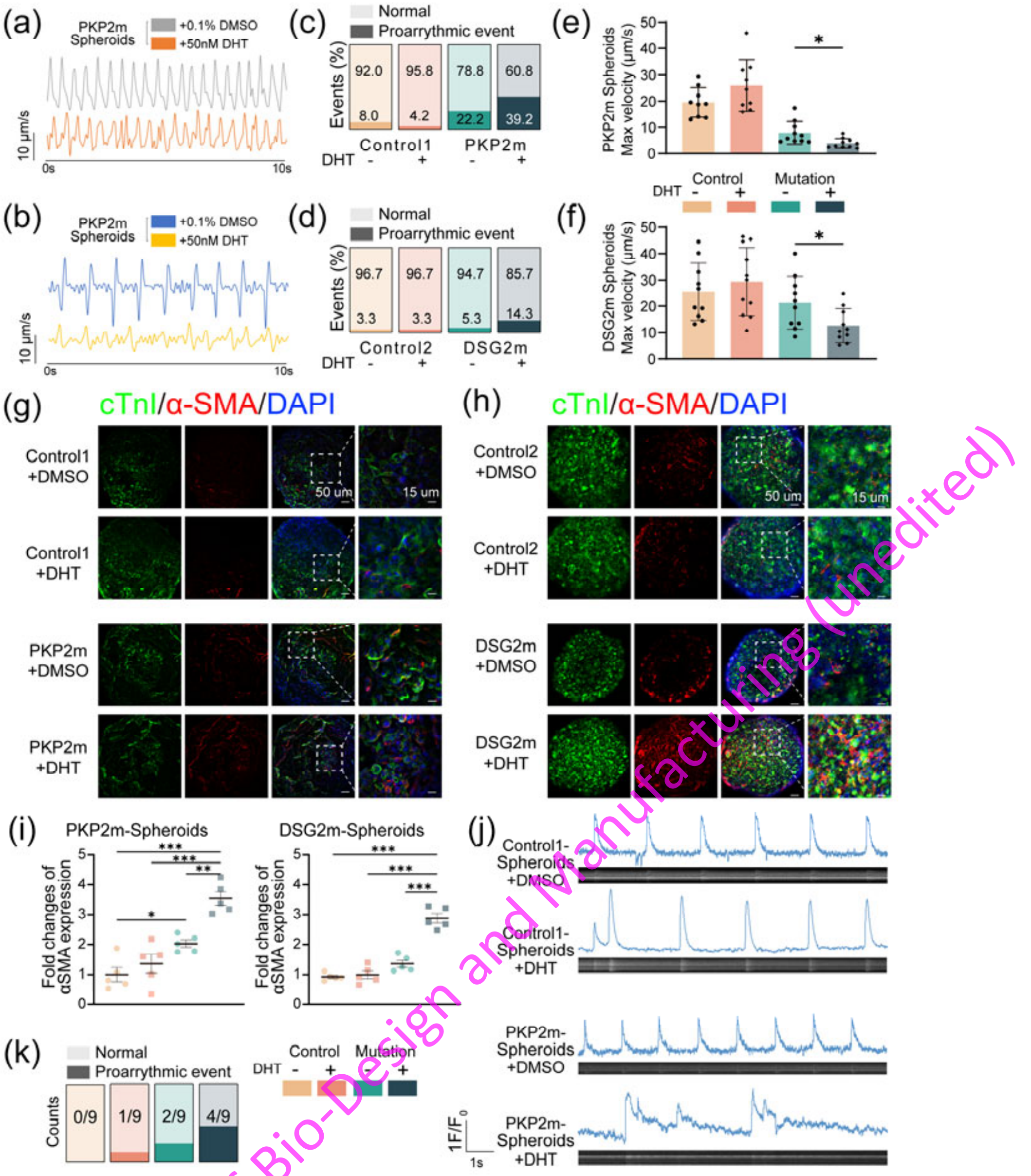

Figure 3 Additional DHT increased proarrhythmic events and fibrosis in ARVC-Spheroids.

(a, b) Representative spontaneous trace of PKP2m-Spheroids and DSG2m-Spheroids, cultured with or without DHT. (c, d) Proportions of proarrhythmic events in PKP2m-Spheroids and DSG2m-Spheroids and corresponding Control-Spheroids, with or without DHT. (e, f) The max velocity of PKP2m-Spheroids and DSG2m-Spheroids and corresponding Control-Spheroids, with or without DHT. *P<0.05. (g, h) Representative immunofluorescence images obtained from PKP2m-Spheroids and DSG2m-Spheroids and corresponding Control-Spheroids, with or without DHT, stained for cTnI (green), α-SMA (red), and DAPI (blue). Bar=50/15(zoom)μm. (i) Quantitative analysis of average α-SMA expression from 5 independent fields. *P<0.05, **P<0.01, ***P<0.001. (j) Representative spontaneous traces of calcium transient of PKP2m-Spheroids. (k) Number of proarrhythmic spheroids treated with or without DHT.

Aberrant pre-mRNA splicing caused by intronic mutations in the PKP2 gene leads to abnormal desmosome complex expression

Mutations in the PKP2 gene are the most common mutation in ARVC, and the mutation site of the PKP2m-iPSC line used in this study is also relatively remarkable [19]. DNA Sanger sequence shows that the mutation site (PKP2 c.336+1G>A) is located at the 3' end of Intron 2 (IVS2) of the PKP2 gene (Figure 4a). Figure 4b demonstrated Sanger sequencing of the reverse-transcribed cDNA, revealing that the c.336+1G>A mutation in the genomic DNA leads to aberrant splicing of the pre-mRNA, skipping the entire Exon2. Figure 4c schematically illustrated the aberrant splicing pattern of the pre-mRNA caused by this intronic mutation. Figure 4d showed the schematic diagram of the pathogenic mechanism of desmosome complex instability and DNA damage caused by PKP2 mutation, and ①~⑤ showed how the mutations can lead to disease. PKP2 protein is located in the intracellular segment of the desmosomes complex. In addition to PKP2, the desmosomes complex also includes transmembrane proteins DSC2 and DSG2 and intracellular proteins DSP, PKG, and others, which ultimately connect to the intracellular cytoskeletal system[20]. The Sring network analysis of PKP2-related proteins reveals that PKP2 is associated with desmosome complexes and other proteins, such as PRKCA, GJA1, and SCN5A, playing roles in signaling pathways, cell connectivity, and arrhythmias, respectively (Figure 4e).

The PKP2 mutation did not significantly alter the mRNA expression of *PKP2*. However, the gene expression of other desmosome genes (*DSP*, *JUP*, *DSC2*, *DSG2*) was upregulated (Figure 4f). This suggested that the structural and functional abnormalities caused by the PKP2 mutation may lead to compensatory upregulation of adjacent desmosomal-related genes. The representative immunofluorescent images showed the distribution of PKP2 on both Control-VCMs and PKP2m-VCMs (Figure 4g). PKP2 protein expression was almost absent in PKP2m-VCMs, while in the Control-VCMs, PKP2 protein was scattered in the cell membrane. Transmission electron microscopy (TEM) images showed the ultrastructure of Control-VCMs and PKP2m-VCMs. (Figure 4h). Compared with Control-VCMs, PKP2m-VCMs have dysplastic sarcomere structure (black arrow) and intracellular lipid droplets (white arrow).

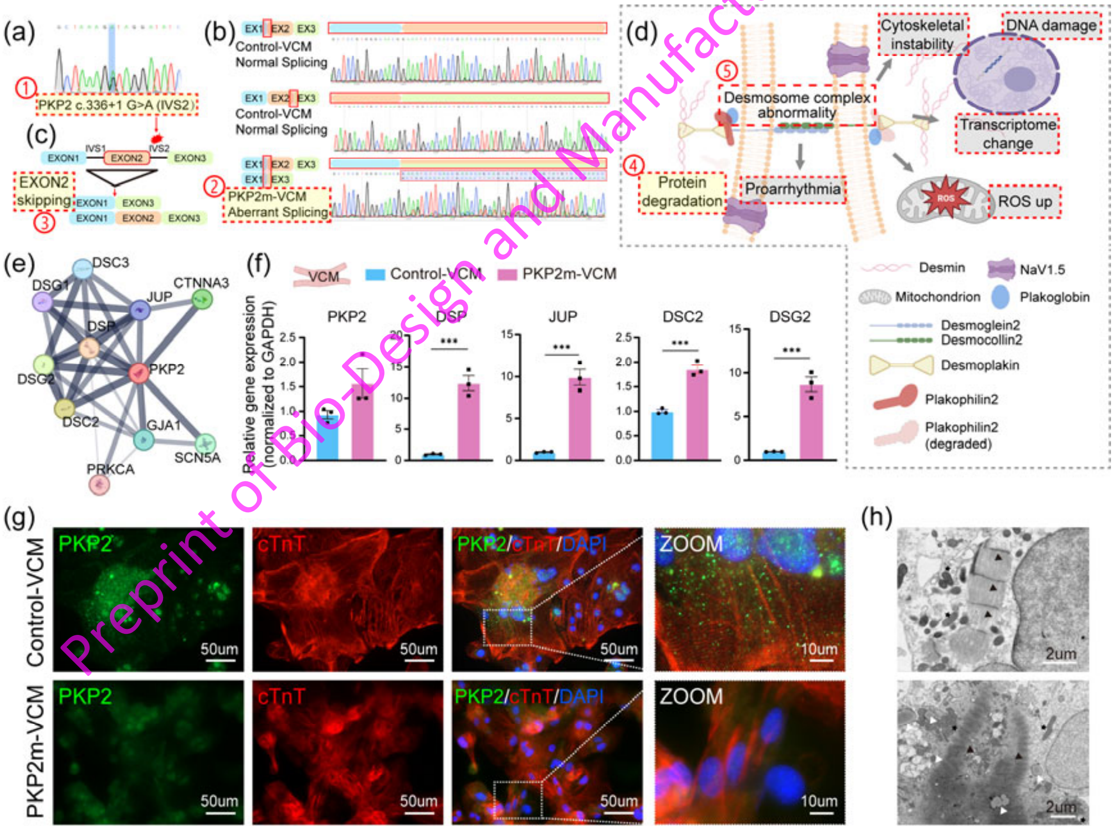

Figure 4 Mutation characterization of iPSC-VCM.

(a) Sanger sequencing of the DNA confirmed the mutation site (PKP2 c.336+1 G>A, IVS2). (b) Sanger sequencing of the cDNA confirmed the splicing mutations within the canonical splice sites leading to whole EXON2 skipping. (c) Schematic diagram of aberrant splicing. (d) Schematic diagram of the pathogenesis of desmosomes complex instability and DNA damage caused by PKP2 mutations. (e) Sring network analysis of

PKP2-related proteins. (f) The relative gene expression of other desmosome genes (DSP, JUP, DSC2, DSG2) except PKP2 were compensatively upregulated. (g) Representative immunofluorescent images showing the distribution of PKP2 on both control-VCMs and PKP2m-VCMs. PKP2 (green), cTnT (red), and DAPI (blue). Bar=50/10(zoom)μm. (h) Representative transmission electron microscopy (TEM) images show the ultrastructure of Control-VCM and PKP2m-VCM. PKP2m-VCM has a dysplastic sarcomere structure and intracellular lipid droplets. The black arrow indicates z-lines, the white arrow indicates lipid droplets, black star arrow indicates mitochondria. Bar=2μm.

DHT increased DNA damage and ROS levels in PKP2m-VCM

To investigate the potential role of DHT in cardiac fibrosis of ARVC, we employed a co-culture model involving VCMs and icFBs in a Transwell system to simulate the intercellular communication present *in vivo* and investigate the pathogenic mechanisms of ARVC. The culture medium was supplemented with or without 50nM DHT. The schematic diagram of this Transwell co-culture experiment is depicted in Figure 5a, while Figure 5b presents the grouping of the experimental conditions.

Mutations in desmosomal proteins can lead to nuclear instability, resulting in DNA damage indicated by the increased γH2AX levels [21]. Immunofluorescence staining of γH2AX in PKP2m-VCMs and Control-VCMs revealed that PKP2m-VCMs exhibited a higher ratio of γH2AX-positive cells compared to Control-VCMs (Figure 5c, d). Furthermore, the percentage of γH2AX-positive cells was further increased in PKP2m-VCMs upon DHT supplementation. These findings suggest that PKP2m-VCMs experienced more pronounced DNA damage than Control-VCMs, and DHT can exacerbate this damage. Increased DNA damage in cardiomyocytes was accompanied by elevated production of ROS (Figure5e). In our study, we observed that both PKP2m-VCMs with and without DHT supplementation exhibited a significant increase in DCF

(2′,7′-dichlorofluorescein) fluorescence intensity compared to the matched Control-VCMs (cCV and cCT). The fold changes in DCF fluorescence intensity were 8.93±1.13 and 10.13±1.29, respectively (Figure 5f).

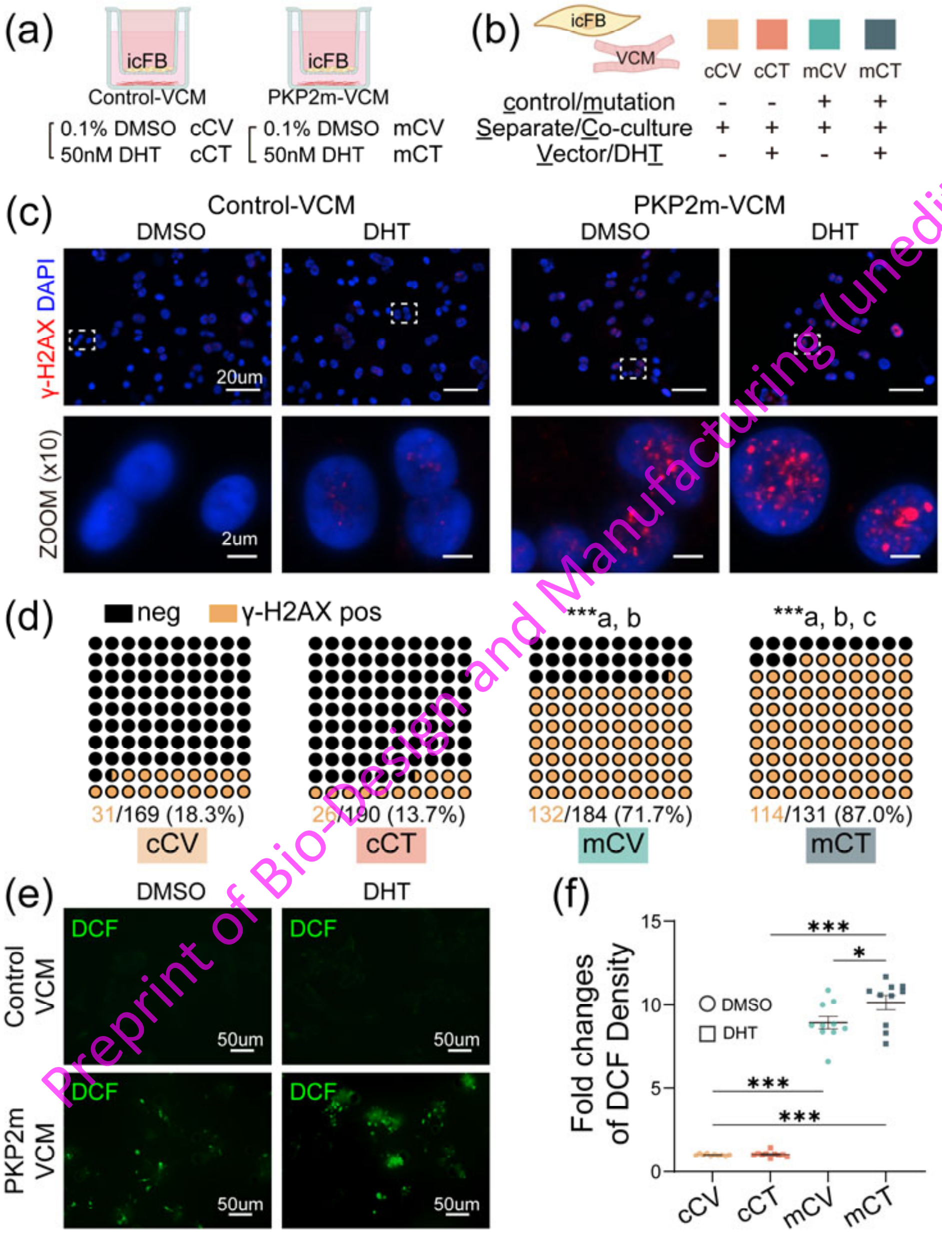

Figure 5 PKP2 mutations and additional DHT lead to DNA damage and ROS up in VCMs.

(a) Diagram of Transwell co-culture between VCMs and icFBs. (b) Grouping diagram of co-culture experiment in the Transwell. The co-cultured VCMs carry PKP2 mutation or not (control/mutation); co-cultured with VCMs or not (Separate/Co-culture); treated with or without 50nm DHT (Vector/DHT). (c) Representative images obtained from control-VCMs and PKP2m-VCMs, with or without 50nM DHT, stained for γH2AX (red) and DAPI (blue). Bar=20/2(zoom)µm. (d) Quantitative analysis of the percentage of γH2AX positive cells from 10 independent fields. ***a, compared with cCV; ***b, compared with cCT; ***c, compared with mCT, ***P<0.001. (e) Representative ROS Assay (DCF) images obtained from control-VCMs and PKP2m-VCMs, with or without 50nM DHT in the medium. Bar=50 µm. (f) Quantitative analysis of DCF fluorescence intensity from 10 independent visual fields (VCMs). *P<0.05, ***P<0.001

icFBs co-cultured with PKP2m-VCMs represent elevated ROS levels, and DHT exacerbated this process.

PKP2m-VCMs represent spontaneous DNA damage. The paracrine pathway of cardiomyocytes and excessive ROS generated by cardiomyocytes can impact the co-cultured icFBs (without mutation). While under the current co-culture conditions, icFBs show no spontaneous DNA damage (Figure 6a, b) but represent ROS up when co-cultured with PKP2m-VCMs. When icFBs were co-cultured with PKP2m-VCMs, the DCF fluorescence intensity of icFBs significantly increased compared to icFBs co-cultured with Control-VCMs, regardless of DHT supplementation (Figure 6c). The fold changes in DCF fluorescence intensity were 5.61±1.20 and 7.26±0.96, respectively (Figure 6d). Notably, PKP2m-icFBs carrying the mutation still showed spontaneous DNA damage and ROS up even when co-cultured with Control-VCMs (Figure 6a, b, c). This may, therefore, may obscure the independent role of DHT. Consistent results were obtained through flow cytometry analysis (Figure 6e, f). Furthermore, within the subset of icFBs co-cultured with PKP2m-VCMs and DHT supplementation, a significant upregulation of DCF fluorescence intensity was observed in a specific subset of icFBs (indicated by the red arrow).

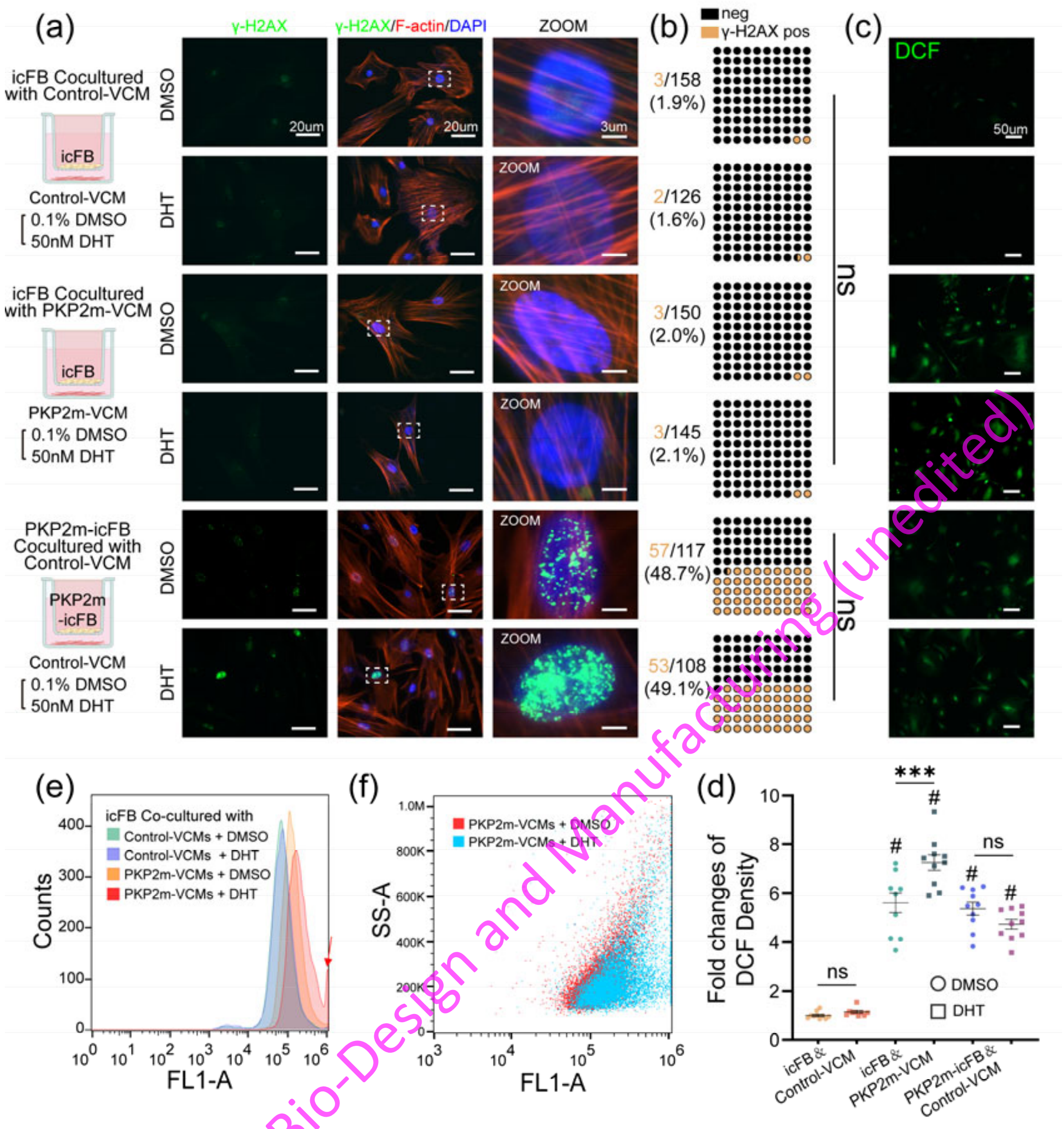

Figure 6 Co-cultured with PKP2m-VCMs and additional DHT lead to DNA damage and increased ROS level in icFBs.

(a) Representative images obtained from icFBs co-cultured with control-VCMs or PKP2m-VCMs, with or without 50nM DHT, and PKP2m-icFBs co-cultured with control-VCMs. stained for γH2AX (green), F-actin (red), and DAPI (blue). Bar=20 μm. (b) Quantitative analysis of the percentage of γH2AX positive cells from 10 independent fields. (c) Representative ROS Assay images obtained from icFBs. (d) Quantitative analysis of DCF fluorescence intensity from 10 independent visual fields (icFBs). ***P<0.001; #, compared with icFBs co-cultured with Control-VCMs, P<0.001. (e, f) Flow cytometry of ROS Assay to analyze the DCF fluorescence intensity of icFBs.

DHT exacerbates the imbalance between anti-inflammatory and pro-

inflammatory responses in the co-culture system and leads to increased myofibroblast activation

To assess the myofibrosis of icFBs in response to co-culture with PKP2m-VCMs and Control-VCMs, we performed α-SMA staining (Figure 7a). Our results revealed a significant increase in α-SMA expression in icFBs co-cultured with PKP2m-VCMs compared to those co-cultured with Control-VCMs. Moreover, additional DHT supplementation further upregulated the expression of α-SMA in icFBs co-cultured with PKP2m-VCMs (Figure 7b, mCV *vs.* mCT). However, no significant changes in α-SMA expression were observed in icFBs co-cultured with Control-VCMs (Figure 7b, cCV *vs.* cCT). Previous studies have reported that cardiomyocytes inhibit fibroblast fibrosis under normal circumstances through the ANP/BNP pathway (13). However, analysis of the concentration of Pro-BNP in the culture medium supernatant did not reveal significant changes (Figure 7c). Additionally, figure 7d demonstrates no significant difference in the expression of *NPPA*/*NPPB* genes between Control-VCMs and PKP2m-VCMs.

Using qPCR, we then quantitatively analyzed fibrosis and inflammation-related mRNA in icFBs (Figure S6). The results indicate that when icFBs were not co-cultured with VCMs, the DHT treatment did not exacerbate fibrosis or upregulate mRNA expression of collagen deposition-related genes. It also did not alter the inflammation levels in icFBs (grey block). However, the situation changed when icFBs were co-cultured separately with Control-VCMs and PKP2m-VCMs. Co-culturing with Control-VCMs led to significant downregulation of several fibrosis-related mRNA (SV *vs* cCV), including *ACTA2*, *COL1A1*, *POSTN*, *DDR2*, *MMP1*, *MMP2*, and *MMP3*. Among the inflammation-related genes, *IL1α*, *IL6*, *TNFα*, and *NFκb* were also significantly downregulated. This suggests that cardiomyocytes exert inhibitory effects on inflammation activation and fibrosis activation in co-cultured fibroblasts. While *COX2* was upregulated, this may be due to the influence of robust myocardial mitochondrial respiration under co-culture conditions. When icFBs were co-cultured with PKP2m-VCMs, PKP2m-VCMs did not exhibit an inhibitory effect on inflammation activation and fibrosis activation (cCV *vs.* mCV), as evident from the increased expression of almost all mentioned genes except *IL1β*.

These findings suggest that the mutation did not weaken the classical ANP/BNP pathway but promoted fibroblast fibrosis through increased ROS levels in the culture system. In the process, the additional DHT exacerbated the imbalance between anti-inflammatory and pro-inflammatory responses in the co-culture system and finally led to an increased myofibroblast activation of icFBs (Figure 7e).

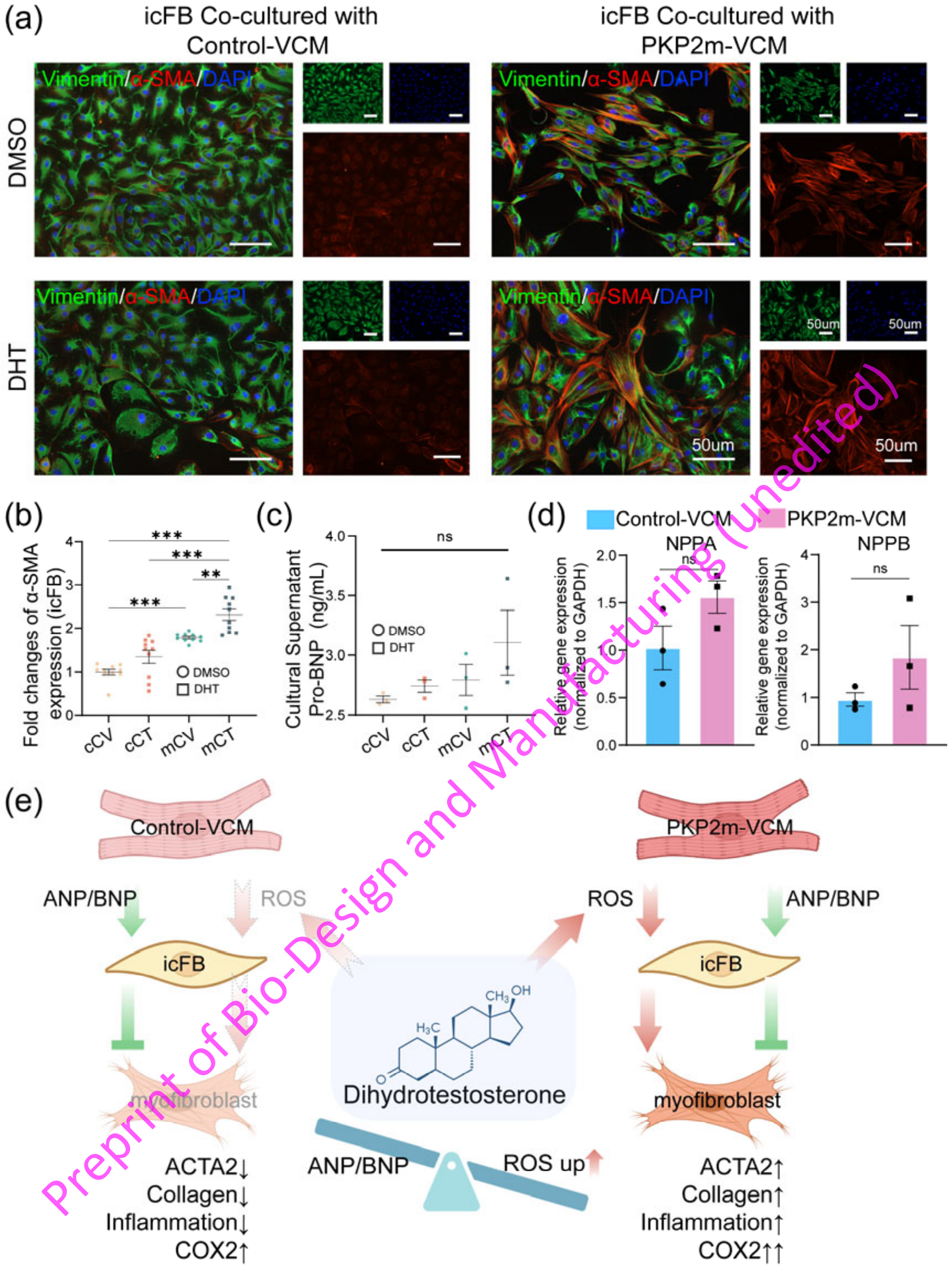

Figure 7 Co-culturing VCM can attenuate or enhance the myofibroblast transformation of icFBs through the ANP/BNP or ROS pathways during co-cultivation.
(a) Representative immunofluorescent images obtained from icFBs co-cultured with control-VCMs or PKP2m-VCMs, with or without 50nM DHT, stained for Vimentin (green), α-SMA (red), and DAPI (blue). Bar=50 μm. (b) Quantitative analysis of average α-SMA expression from 10 independent fields. $^{**}P<0.01$, $^{***}P<0.001$. (c) The content of pro-BNP in the supernatant of cell culture medium in the Transwell. (d) Expression of NPPA/NPPB genes in the Control-VCM and PKP2m-VCM. (e)

Schematic diagram of the effect of DHT and co-cultured VCMs on icFBs during co-cultivation. Light red dotted arrows represent lower ROS levels.

Discussion

Cardiac fibrosis in ARVC patients provided the abnormal substrate for arrhythmias maintenance, and we have reported that achieving electrical isolation of the right ventricular free wall (RVFW) is a feasible option for late-phase patients[22]. Therefore, it is essential to elucidate the potential contributors to the progression of myocardial fibrosis to understand the disease better.

In this study, we observed that gender differences impact the area of low-voltage zones detected in the electrophysiological mapping of patients' hearts with ARVC. Multiple studies have found that compared to females, males have a higher relative risk (1.6 to 3.2 times) of ARVC[23-28]. This effect appears to be partially associated with differences in sex hormones. Testosterone enhances the ARVC phenotype and increases cardiac-related events, while estradiol has a protective effect[6]. Previous studies have suggested that elevated testosterone levels contribute to disease progression in ARVC patients[6, 29]. An epidemiological researchs has also demonstrated that increased testosterone levels are associated with a higher incidence of arrhythmic events and MACE in ARVC patients[30]. One possible mechanism is that testosterone exacerbates cardiomyocyte apoptosis in ARVC[6]. However, a causal relationship between testosterone and the aggravation of fibrosis has not been well established in ARVC.

Testosterone exerts different effects on the process of cardiac fibrosis. Previous studies have shown that testosterone can attenuate the activation of cardiac fibroblasts in rats by modulating TGFβ and AngII signaling pathways[31]. Exogenous testosterone has been found to alleviate cardiac fibrosis and cell apoptosis in Axl-knockout mice[32]. However, testosterone can exacerbate age-related cardiac and renal fibrosis[33]. In addition, the debate regarding testosterone replacement therapy (TRT) in older men continues[34]. On the other hand, Elisa Giacomelli *et al.* [10] demonstrated that spheroids constructed with normal iPSC-VCMs and icFBs obtained from ARVC patients carrying PKP2 mutations exhibited arrhythmic behavior *in vitro*, indicating the pathogenicity of mutated icFBs. Our present study also found spontaneous DNA damage and ROS up in PKP2m-icFBs. In the co-culture system and spheroids with normal icFBs. It demonstrated that DHT exacerbates fibrosis by inducing the excessive release of ROS from mutant cardiomyocytes, leading to the upregulation of inflammatory markers in icFBs, ultimately resulting in fibrosis. DHT can cause more severe nuclear damage and increased ROS release in PKP2m-VCMs, which may be related to the instability of cell membrane-cytoskeleton-nuclear connections caused by desmosomal gene mutations[35]. In the present study, DHT alone did not significantly affect fibrotic marker expression in icFBs. The changes occurred only in the presence of mutant cardiomyocytes, indicating that mutant cardiomyocytes act as the trigger, with testosterone pulling the trigger of DNA damage and ROS production, while fibroblasts, which undergo fibrosis, serve as the scapegoat during the pathogenesis of ARVC.

Interstitial fibrosis contributes to arrhythmogenesis by slowing action potential propagation, facilitating reentry, promoting post-depolarization, and increasing ectopic automaticity *in vivo* [36]. Standard single-cell monolayer *in vitro* models can partially recapitulate 2D arrhythmia phenotypes, such as reentry and rotor formation[37, 38]. However, the 2D models lack hierarchical structures and the representation of multiple cell types, which limits their comprehensiveness and representativeness. Therefore, the use of tissue engineering to construct 3D models with various cell types has become an excellent approach for studying arrhythmias. In the spheroid models, cardiomyocytes derived from iPSCs exhibit greater physiological maturity than monolayer cultures, with aligned sarcomeres, enhanced calcium handling, and improved contractility and electrophysiology[39]. In the present study, our spheroid models exhibited phenotypes including impaired contraction mode, arrhythmogenesis, and fibrosis, which enables researchers to gain a multicellular perspective on ARVC and identify potential therapeutic targets.

In addition to spheroid models, non-animal models (NAMs) have become state-of-the-art for in vitro testing. Including but not limited to cell micropatterning[40, 41], fabricated cardiac microtissues[15, 42-44]. and 3D-printed functional cardiac tissue[45-47]. Although spheroids in this study can simulate cell-cell interactions in 3D culture, this model still has some limitations. For example, it does not have a microfluidic perfusion system, which may lead to insufficient cardiomyocyte maturation in spheroids. In addition, if no engineering strategy like engineered cardiac tissue is adopted[48], the simple spheroids cannot reflect the direction and strength of the contraction well. Therefore, more advanced tissue engineering models are still needed in the future to explain the diverse phenotypes and complex mechanisms of diseases.

Conclusions

In conclusion, our findings provide the first direct evidence *in vitro* of the fibrogenic effect of testosterone in ARVC. Furthermore, we demonstrate the feasibility of utilizing human iPSC-derived engineered cardiac spheroids platforms for modeling genetic cardiomyopathies and conducting drug screening.

Acknowledgments

The research was supported by the National Natural and Science Foundation of China (Grant No. 82370322 to Chang Cui, 82200352 to Feng Zhang, 82300352 to Yue Zhu, 22275034 to Hua Xu and 82070343 to Minglong Chen), the Natural Science Foundation of Jiangsu Province of China (Grant No. BK20220710 to Feng Zhang) and Postgraduate Research & Practice Innovation Program of Jiangsu Province (JX13414086 to Hongyi Cheng).

Author contributions

Chang Cui and Xiaohong Jiang initiated and supervised the project. Hongyi Cheng, Xinrui Wang, and Sichong Qian designed the research. Hongyi Cheng and Feng Zhang performed most of the biochemical and molecular experiments with the assistance of Xinrui Wang and Bingyu Zheng. Yike Zhang, Jincheng Jiao and Yue Zhu contributed to the statistical analysis of clinical data. Xinrui Wang and Sichong Qian contributed to the access to cell resources. Hongyi Cheng wrote the manuscript. Jia Song and Feng

Zhang revised the manuscript. Hongyi Cheng, Yue Zhu, Hua Xu, Feng Zhang, Chang Cui, and Minglong Chen contributed to the funding acquisition.

Declarations

Conflict of interest The authors declared no potential conflicts of interest concerning the research, authorship, and/or publication of this article.

Ethical approval This study was approved by the ethics committee of the First Affiliated Hospital of Nanjing Medical University (approval number: 2022-SR-184).

References

[1] A.D. Krahn, A.A.M. Wilde, H. Calkins, A. La Gerche, J. Cadrin-Tourigny, J.D. Roberts, H.C. Han, Arrhythmogenic Right Ventricular Cardiomyopathy, JACC. Clinical electrophysiology 8(4) (2022) 533-553.

[2] A. Te Riele, C.A. James, A.C. Sawant, A. Bhonsale, J.A. Groeneweg, T.P. Mast, B. Murray, C. Tichnell, D. Dooijes, J.P. van Tintelen, D.P. Judge, J.F. van der Heijden, J. Crosson, R.N.W. Hauer, H. Calkins, H. Tandri, Arrhythmogenic Right Ventricular Dysplasia/Cardiomyopathy in the Pediatric Population: Clinical Characterization and Comparison With Adult-Onset Disease, JACC. Clinical electrophysiology 1(6) (2015) 551-560.

[3] A. Bhonsale, A. Te Riele, A.C. Sawant, J.A. Groeneweg, C.A. James, B. Murray, C. Tichnell, T.P. Mast, M.J. van der Pols, M.J.M. Cramer, D. Dooijes, J.F. van der Heijden, H. Tandri, J.P. van Tintelen, D.P. Judge, R.N.W. Hauer, H. Calkins, Cardiac phenotype and long-term prognosis of arrhythmogenic right ventricular cardiomyopathy/dysplasia patients with late presentation, Heart rhythm 14(6) (2017) 883-891.

[4] N.A. Gilotra, A. Bhonsale, C.A. James, A.S.J. Te Riele, B. Murray, C. Tichnell, A. Sawant, C.S. Ong, D.P. Judge, S.D. Russell, H. Calkins, R.J. Tedford, Heart Failure Is Common and Under-Recognized in Patients With Arrhythmogenic Right Ventricular Cardiomyopathy/Dysplasia, Circulation. Heart failure 10(9) (2017).

[5] A. Azaouagh, S. Churzidse, T. Konorza, R. Erbel, Arrhythmogenic right ventricular cardiomyopathy/dysplasia: a review and update, Clinical research in cardiology : official journal of the German Cardiac Society 100(5) (2011) 383-94.

[6] D. Akdis, A.M. Saguner, K. Shah, C. Wei, A. Medeiros-Domingo, A. von Eckardstein, T.F. Lüscher, C. Brunckhorst, H.S.V. Chen, F. Duru, Sex hormones affect outcome in arrhythmogenic right ventricular cardiomyopathy/dysplasia: from a stem cell derived cardiomyocyte-based model to clinical biomarkers of disease outcome, European heart journal 38(19) (2017) 1498-1508.

[7] P. Chen, Y. Xiao, Y. Wang, Z. Zheng, L. Chen, X. Yang, J. Li, W. Wu, S. Zhang, Intracellular calcium

current disorder and disease phenotype in OBSCN mutant iPSC-based cardiomyocytes in arrhythmogenic right ventricular cardiomyopathy, Theranostics 10(24) (2020) 11215-11229.

[8] C. Kim, J. Wong, J. Wen, S. Wang, C. Wang, S. Spiering, N.G. Kan, S. Forcales, P.L. Puri, T.C. Leone, J.E. Marine, H. Calkins, D.P. Kelly, D.P. Judge, H.S. Chen, Studying arrhythmogenic right ventricular dysplasia with patient-specific iPSCs, Nature 494(7435) (2013) 105-10.

[9] E.C. James, E. Tomaskovic-Crook, J.M. Crook, Bioengineering Clinically Relevant Cardiomyocytes and Cardiac Tissues from Pluripotent Stem Cells, International journal of molecular sciences 22(6) (2021).

[10] E. Giacomelli, V. Meraviglia, G. Campostrini, A. Cochrane, X. Cao, R.W.J. van Helden, A. Krotenberg Garcia, M. Mircea, S. Kostidis, R.P. Davis, B.J. van Meer, C.R. Jost, A.J. Koster, H. Mei, D.G. Míguez, A.A. Mulder, M. Ledesma-Terrón, G. Pompilio, L. Sala, D.C.F. Salvatori, R.C. Slieker, E. Sommariva, A.A.F. de Vries, M. Giera, S. Semrau, L.G.J. Tertoolen, V.V. Orlova, M. Bellin, C.L. Mummery, Human-iPSC-Derived Cardiac Stromal Cells Enhance Maturation in 3D Cardiac Microtissues and Reveal Non-cardiomyocyte Contributions to Heart Disease, Cell stem cell 26(6) (2020) 862-879.e11.

[11] P.H. Zushin, S. Mukherjee, J.C. Wu, FDA Modernization Act 2.0: transitioning beyond animal models with human cells, organoids, and AI/ML-based approaches, The Journal of clinical investigation 133(21) (2023).

[12] J. Bao, J. Wang, Y. Yao, Y. Wang, X. Fan, K. Sun, D.S. He, F.I. Marcus, S. Zhang, R. Hui, L. Song, Correlation of ventricular arrhythmias with genotype in arrhythmogenic right ventricular cardiomyopathy, Circulation. Cardiovascular genetics 6(6) (2013) 552-6.

[13] Y. Zhu, L. Wang, C. Cui, H. Qin, H. Chen, S. Chen, Y. Lin, H. Cheng, X. Jiang, M. Chen, Pathogenesis and drug response of iPSC-derived cardiomyocytes from two Brugada syndrome patients with different Na (v)1.5-subunit mutations, Journal of biomedical research 35(5) (2021) 395-407.

[14] H. Zhang, L. Tian, M. Shen, C. Tu, H. Wu, M. Gu, D.T. Paik, J.C. Wu, Generation of Quiescent Cardiac Fibroblasts From Human Induced Pluripotent Stem Cells for In Vitro Modeling of Cardiac Fibrosis, Circulation research 125(5) (2019) 552-566.

[15] F. Zhang, H. Cheng, K. Qu, X. Qian, Y. Lin, Y. Zhang, S. Qian, N. Huang, C. Cui, M. Chen, Continuous contractile force and electrical signal recordings of 3D cardiac tissue utilizing conductive hydrogel pillars on a chip, Materials today. Bio 20 (2023) 100626.

[16] N. Huebsch, P. Loskill, M.A. Mandegar, N.C. Marks, A.S. Sheehan, Z. Ma, A. Mathur, T.N. Nguyen, J.C. Yoo, L.M. Judge, C.I. Spencer, A.C. Chukka, C.R. Russell, P.L. So, B.R. Conklin, K.E. Healy, Automated Video-Based Analysis of Contractility and Calcium Flux in Human-Induced Pluripotent Stem Cell-Derived Cardiomyocytes Cultured over Different Spatial Scales, Tissue engineering. Part C, Methods 21(5) (2015) 467-79.

[17] F. Zhang, K.Y. Qu, B. Zhou, Y. Luo, Z. Zhu, D.J. Pan, C. Cui, Y. Zhu, M.L. Chen, N.P. Huang, Design and fabrication of an integrated heart-on-a-chip platform for construction of cardiac tissue from human iPSC-derived cardiomyocytes and in situ evaluation of physiological function, Biosensors & bioelectronics 179 (2021) 113080.

[18] D. Albanese, M. Filosi, R. Visintainer, S. Riccadonna, G. Jurman, C. Furlanello, Minerva and minepy: a C engine for the MINE suite and its R, Python and MATLAB wrappers, Bioinformatics (Oxford, England) 29(3) (2013) 407-8.

[19] E. Gandjbakhch, A. Redheuil, F. Pousset, P. Charron, R. Frank, Clinical Diagnosis, Imaging, and

Genetics of Arrhythmogenic Right Ventricular Cardiomyopathy/Dysplasia: JACC State-of-the-Art Review, Journal of the American College of Cardiology 72(7) (2018) 784-804.

[20] S.H. Vermij, H. Abriel, T.A. van Veen, Refining the molecular organization of the cardiac intercalated disc, Cardiovascular research 113(3) (2017) 259-275.

[21] M.S. Siddiqui, M. François, M.F. Fenech, W.R. Leifert, Persistent γH2AX: A promising molecular marker of DNA damage and aging, Mutation research. Reviews in mutation research 766 (2015) 1-19.

[22] N. Wu, H. Chen, W. Ju, M. Li, K. Gu, Z. Wang, H. Liu, J. Shi, X. Jiang, C. Cui, C. Cai, G. Yang, M. Chen, Arrhythmogenic Right Ventricular Cardiomyopathy With Extensive Abnormal Substrate: Is Isolation Possible?, JACC. Clinical electrophysiology (2023).

[23] A. Bhonsale, C.A. James, C. Tichnell, B. Murray, S. Madhavan, B. Philips, S.D. Russell, T. Abraham, H. Tandri, D.P. Judge, H. Calkins, Risk stratification in arrhythmogenic right ventricular dysplasia/cardiomyopathy-associated desmosomal mutation carriers, Circulation. Arrhythmia and electrophysiology 6(3) (2013) 569-78.

[24] I. Rigato, B. Bauce, A. Rampazzo, A. Zorzi, K. Pilichou, E. Mazzotti, F. Migliore, M.P. Marra, A. Lorenzon, M. De Bortoli, M. Calore, A. Nava, L. Daliento, D. Gregori, S. Iliceto, G. Thiene, C. Basso, D. Corrado, Compound and digenic heterozygosity predicts lifetime arrhythmic outcome and sudden cardiac death in desmosomal gene-related arrhythmogenic right ventricular cardiomyopathy, Circulation. Cardiovascular genetics 6(6) (2013) 533-42.

[25] A. Mazzanti, K. Ng, A. Faragli, R. Maragna, E. Chiodaroli, N. Orphanou, N. Monteforte, M. Memmi, P. Gambelli, V. Novelli, R. Bloise, O. Catalano, G. Moro, V. Tibollo, M. Morini, R. Bellazzi, C. Napolitano, V. Bagnardi, S.G. Priori, Arrhythmogenic Right Ventricular Cardiomyopathy: Clinical Course and Predictors of Arrhythmic Risk, Journal of the American College of Cardiology 68(23) (2016) 2540-2550.

[26] A. Martin, J. Crawford, J.R. Skinner, W. Smith, High Arrhythmic Burden but Low Mortality during Long-term Follow-up in Arrhythmogenic Right Ventricular Cardiomyopathy, Heart, lung & circulation 25(3) (2016) 275-81.

[27] Y. Kimura, T. Noda, Y. Otsuka, M. Wada, I. Nakajima, K. Ishibashi, K. Miyamoto, H. Okamura, T. Aiba, S. Kamakura, T. Noguchi, T. Anzai, K. Satomi, H. Ogawa, S. Yasuda, K.F. Kusano, Potentially Lethal Ventricular Arrhythmias and Heart Failure in Arrhythmogenic Right Ventricular Cardiomyopathy: What Are the Differences Between Men and Women?, JACC. Clinical electrophysiology 2(5) (2016) 546-555.

[28] C.Y. Lin, F.P. Chung, Y.J. Lin, S.L. Chang, L.W. Lo, Y.F. Hu, T.C. Tuan, T.F. Chao, J.N. Liao, Y.T. Chang, Y.Y. Chen, R. Walia, A.L.D. Te, S. Yamada, S.A. Chen, Gender differences in patients with arrhythmogenic right ventricular dysplasia/cardiomyopathy: Clinical manifestations, electrophysiological properties, substrate characteristics, and prognosis of radiofrequency catheter ablation, International journal of cardiology 227 (2017) 930-937.

[29] J. Ren, L. Chen, N. Zhang, X. Chen, Q. Zhao, K. Chen, X. Li, F. Ruschitzka, F. Duru, J. Song, Plasma testosterone and arrhythmic events in male patients with arrhythmogenic right ventricular cardiomyopathy, ESC heart failure 7(4) (2020) 1547-1559.

[30] B.B. Yeap, R.J. Marriott, L. Antonio, S. Raj, G. Dwivedi, C.M. Reid, B.D. Anawalt, S. Bhasin, A.S. Dobs, D.J. Handelsman, G.J. Hankey, R. Haring, A.M. Matsumoto, P.E. Norman, T.W. O'Neill, C. Ohlsson, E.S. Orwoll, D. Vanderschueren, G.A. Wittert, F.C.W. Wu, K. Murray, Associations of Serum Testosterone and Sex Hormone-Binding Globulin With Incident Cardiovascular Events in Middle-

Aged to Older Men, Annals of internal medicine 175(2) (2022) 159-170.

[31] C.C. Chung, R.C. Hsu, Y.H. Kao, J.P. Liou, Y.Y. Lu, Y.J. Chen, Androgen attenuates cardiac fibroblasts activations through modulations of transforming growth factor-β and angiotensin II signaling, International journal of cardiology 176(2) (2014) 386-93.

[32] F.F. Chen, F.Q. Song, Y.Q. Chen, Z.H. Wang, Y.H. Li, M.H. Liu, Y. Li, M. Song, W. Zhang, J. Zhao, M. Zhong, Exogenous testosterone alleviates cardiac fibrosis and apoptosis via Gas6/Axl pathway in the senescent mice, Experimental gerontology 119 (2019) 128-137.

[33] T.D. Hewitson, C. Zhao, B. Wigg, S.W. Lee, E.R. Simpson, W.C. Boon, C.S. Samuel, Relaxin and castration in male mice protect from, but testosterone exacerbates, age-related cardiac and renal fibrosis, whereas estrogens are an independent determinant of organ size, Endocrinology 153(1) (2012) 188-99.

[34] R.A. Kloner, C. Carson, 3rd, A. Dobs, S. Kopecky, E.R. Mohler, 3rd, Testosterone and Cardiovascular Disease, Journal of the American College of Cardiology 67(5) (2016) 545-57.

[35] M. Pérez-Hernández, C.J.M. van Opbergen, N. Bagwan, C.R. Vissing, G.M. Marrón-Liñares, M. Zhang, E. Torres Vega, A. Sorrentino, L. Drici, K. Sulek, R. Zhai, F.B. Hansen, A.H. Christensen, S. Boesgaard, F. Gustafsson, K. Rossing, E.M. Small, M.J. Davies, E. Rothenberg, P.Y. Sato, M. Cerrone, T.H.L. Jensen, K. Qvortrup, H. Bundgaard, M. Delmar, A. Lundby, Loss of Nuclear Envelope Integrity and Increased Oxidant Production Cause DNA Damage in Adult Hearts Deficient in PKP2: A Molecular Substrate of ARVC, Circulation 146(11) (2022) 851-867.

[36] M.N. Nguyen, H. Kiriazis, X.M. Gao, X.J. Du, Cardiac Fibrosis and Arrhythmogenesis, Comprehensive Physiology 7(3) (2017) 1009-1049.

[37] N. Harlaar, S.O. Dekker, J. Zhang, R.R. Snabel, M.W. Veldkamp, A.O. Verkerk, C.C. Fabres, V. Schwach, L.J.S. Lerink, M.R. Rivaud, A.A. Mulder, W.E. Corver, M. Goumans, D. Dobrev, R.J.M. Klautz, M.J. Schalij, G.J.C. Veenstra, R. Passier, T.J. van Brakel, D.A. Pijnappels, A.A.F. de Vries, Conditional immortalization of human atrial myocytes for the generation of in vitro models of atrial fibrillation, Nature biomedical engineering 6(4) (2022) 389-402.

[38] N. Shaheen, A. Shiti, I. Huber, R. Shinnawi, G. Arbel, A. Gepstein, N. Setter, I. Goldfracht, A. Gruber, S.V. Chorna, L. Gepstein, Human Induced Pluripotent Stem Cell-Derived Cardiac Cell Sheets Expressing Genetically Encoded Voltage Indicator for Pharmacological and Arrhythmia Studies, Stem cell reports 10(6) (2018) 1879-1894.

[39] A.H. Sadeghi, S.R. Shin, J.C. Deddens, G. Fratta, S. Mandla, I.K. Yazdi, G. Prakash, S. Antona, D. Demarchi, M.P. Buijsrogge, J.P.G. Sluijter, J. Hjortnaes, A. Khademhosseini, Engineered 3D Cardiac Fibrotic Tissue to Study Fibrotic Remodeling, Advanced healthcare materials 6(11) (2017).

[40] K. Zhang, P.E. Cloonan, S. Sundaram, F. Liu, S.L. Das, J.K. Ewoldt, J.L. Bays, S. Tomp, C.N. Toepfer, J.D.C. Marsiglia, J. Gorham, D. Reichart, J. Eyckmans, J.G. Seidman, C.E. Seidman, C.S. Chen, Plakophilin-2 truncating variants impair cardiac contractility by disrupting sarcomere stability and organization, Science advances 7(42) (2021) eabh3995.

[41] A. Eguchi, A. Gonzalez, S.I. Torres-Bigio, K. Koleckar, F. Birnbaum, J.Z. Zhang, V.Y. Wang, J.C. Wu, S.E. Artandi, H.M. Blau, TRF2 rescues telomere attrition and prolongs cell survival in Duchenne muscular dystrophy cardiomyocytes derived from human iPSCs, Proceedings of the National Academy of Sciences of the United States of America 120(6) (2023) e2209967120.

[42] E.Y. Wang, N. Rafatian, Y. Zhao, A. Lee, B.F.L. Lai, R.X. Lu, D. Jekic, L. Davenport Huyer, E.J. Knee-Walden, S. Bhattacharya, P.H. Backx, M. Radisic, Biowire Model of Interstitial and Focal Cardiac Fibrosis, ACS central science 5(7) (2019) 1146-1158.

[43] R.K. Jayne, M. Karakan, K. Zhang, N. Pierce, C. Michas, D.J. Bishop, C.S. Chen, K.L. Ekinci, A.E. White, Direct laser writing for cardiac tissue engineering: a microfluidic heart on a chip with integrated transducers, Lab on a chip 21(9) (2021) 1724-1737.

[44] K. Williams, T. Liang, S. Massé, S. Khan, R. Hatkar, G. Keller, K. Nanthakumar, S.S. Nunes, A 3-D human model of complex cardiac arrhythmias, Acta biomaterialia 132 (2021) 149-161.

[45] U. Yong, D. Kim, H. Kim, D.G. Hwang, S. Cho, H. Nam, S. Kim, T. Kim, U. Jeong, K. Kim, W.K. Chung, W.H. Yeo, J. Jang, Biohybrid 3D Printing of a Tissue-Sensor Platform for Wireless, Real-Time, and Continuous Monitoring of Drug-Induced Cardiotoxicity, Advanced materials (Deerfield Beach, Fla.) 35(11) (2023) e2208983.

[46] S. Liu, Z. Wang, X. Chen, M. Han, J. Xu, T. Li, L. Yu, M. Qin, M. Long, M. Li, H. Zhang, Y. Li, L. Wang, W. Huang, Y. Wu, Multiscale Anisotropic Scaffold Integrating 3D Printing and Electrospinning Techniques as a Heart-on-a-Chip Platform for Evaluating Drug-Induced Cardiotoxicity, Advanced healthcare materials 12(24) (2023) e2300719.

[47] Y.S. Zhang, A. Arneri, S. Bersini, S.R. Shin, K. Zhu, Z. Goli-Malekabadi, J. Aleman, C. Colosi, F. Busignani, V. Dell'Erba, C. Bishop, T. Shupe, D. Demarchi, M. Moretti, M. Rasponi, M.R. Dokmeci, A. Atala, A. Khademhosseini, Bioprinting 3D microfibrous scaffolds for engineering endothelialized myocardium and heart-on-a-chip, Biomaterials 110 (2016) 45-59.

[48] J. Cho, H. Lee, W. Rah, H.J. Chang, Y.S. Yoon, From engineered heart tissue to cardiac organoid, Theranostics 12(6) (2022) 2758-2772.